The Stern-Gerlach Spectrometer for Charged Particles

A step towards an alternative method for measuring spin

Samuel Eriksson

A thesis presented for the degree of
Bachelor of Science

Supervisor:
Mathieu Gisselbrecht

Project duration: 2 months
Division of Synchrotron Radiation
Department of Physics
Lund University
January 2023

Abstract

The purpose of this project is to investigate the performance of a spectrometer capable of measuring both momentum and spin of particles. More specifically, we investigated what parameters are required in order to separate particles with opposite spins at least $1\,\mathrm{mm}$. This project can serve as the first step in the process of building such a spectrometer.

This spectrometer takes the core principles of the Stern-Gerlach device and the modern time-of-flight spectrometer and combines them in order to measure spin in an alternative way; the device would contain, extract and measure particles in the same manner as the time-of-flight spectrometer. However, it would do so by using an inhomogeneous magnetic field rather than a homogeneous one. This separates particles with spin up and down, similar to what was done in the original Stern-Gerlach experiment.

During this project, a numerical simulation was developed to identify and test the simplest, realistic design. It was discovered that helium ions require a time of flight of $\sim 1\,\mathrm{ms}$ in order to reach a $1\,\mathrm{mm}$ spin separation. In this case, a light source with a repetition rate of $1\,\mathrm{kHz}$ or slower is required for operation. For electrons, it was found that they require a time of flight $\sim 10\,\mu\mathrm{s}$ in order to achieve the target separation. In this case, the upper limit on the repetition rate of the light source is $100\,\mathrm{kHz}$. Lastly, a set of prescriptions were made for how to improve the simulation and how to operate the device under different conditions.

Acknowledgements

I would like to thank Amanda Arvidsson for all of her love and support, even through the toughest of times. I would like to thank Mathieu Gisselbrecht, not only for guiding me through the process of writing this thesis, but for also giving me the courage to pursue a dream I had all but given up on. I would like to thank Ola Jentzsch and Niklas Fröjd for unlocking a passion I did not know I had. If there is even one iota of eloquence contained within this text, it is thanks to them.

These people helped in ways that may have seemed small, but in the end they had a tremendous impact on the trajectory of my life. Were it not for the convergence of their efforts, this work, my first addition to the ever growing body of science, would never have been possible. I will always remember and cherish the things they did for me.

Contents

1 Introduction

1.1 Motivation

At the time of writing, the most recent Nobel prize in physics was awarded to Alain Aspect, John Clauser and Anton Zeilinger for their work with entangled photons. It is clear that entanglement in quantum information is a growing field of study and so new techniques for the measurement of entanglement between massive particles is becoming of importance. One relevant line of inquiry is how can entanglement of charged particles be measured? More specifically: Is it possible to measure the entanglement in spin between electrons and ions created by photoionization?

The spin of massive particles was experimentally discovered by Otto Stern and Walter Gerlach one century ago. In their experiment, a beam of neutral atoms was deflected by a strong in-homogeneous magnetic field, revealing that atoms possess a magnetic moment. In the case of silver atoms, this magnetic moment could only originate from the spin angular momentum of the valence electron.

The spin of the electron upon photoionization is usually investigated with a Mott spin-polarimeter [1]. In this setup, an electron beam of uncertain polarity is scattered off a solid state target, usually made of gold, who acts as a polarimeter. Due to spin-orbit coupling, the scattering potential will not be the same for different spin polarities and the scattering angle will differ, achieving thereby a spin separation in space. Hence the electron beams with different spins can be analysed. This approach is used at synchrotron facilities, for instance at the BLOCH beamline of the MAX-IV laboratory for material science. However, this method suffers from a very low efficiency since most of the electrons are not scattered by the target, and efforts are made to improve this instrument by developing new design or fabricating new solid target material [2].

For measuring the spin of the ions, the Penning trap is often used for high precision measurements of the magnetic moments [3, 4]. This trap confines particles with electrostatic and magnetostatic fields, a technique which has proven successful for measuring g-factors [5]. However, in the process of enclosing the particles inside the trap they are removed from any prior context and so this method cannot easily take measurements in dynamic situations, such as ionization event at a high repetition rate of 1kHz.

Over the past two decades, the development of charged particle spectrometers in the field of atomic and molecular physics has made it possible to measure not only the kinetic energy of the electron or the mass of the ions but also the momentum of these particles. To this end, the spectrometers are equipped with specialized detectors which can measure both the impact position and the time of flight simultaneously. With the help of a homogeneous electric extraction field, sometimes paired with a homogeneous magnetic field for confinement, the complete kinematics of emitted electrons and ions can be determined. As these charged particles have a magnetic moment, a natural extension of these spectrometers could be to use an inhomogeneous magnetic field, with a strong gradient, to measure the spin of electrons and ions. This approach would be similar to the method seen in the Stern-Gerlach experiment but, crucially, it could work for charged particles rather than a neutral atomic beam.

However, studying charged particles in this manner presents a substantial challenge. Indeed, given a $1\,\mathrm{T}$ magnetic field, a singly charged ion moving with a thermal speed around $500 - 1000\,\mathrm{m/s}$ would feel a Lorentz force of $10^{-16}\,\mathrm{N}$. On the other hand, the force due to the interaction between the spin magnetic moment and the gradient of an inhomogeneous magnetic field, assuming a gradient around $\sim 1\,\mathrm{T/cm}$, is only around $10^{-22}\,\mathrm{N}$. In this case, the Lorentz force dominates by 6 orders of magnitude, which illustrates the difficulty with this type of measurement. In order to use this principle to measure the spin, the force acting on the spin must be distinguished from a force upwards of one million times stronger.

The aim of this project is to numerically explore the trajectories of charged particles as they interact with the combined Lorentz-Stern-Gerlach force. Ultimately, this study should be able to identify the range of parameters that are feasible and what types of constraints are required in order to simultaneously measure the spin of electrons and ions.

1.2 Background

In the following sections, the principle of modern time-of-flight spectrometer, used in atomic and molecular physics, is explained as well at the original Stern-Gerlach apparatus. Lastly, these ideas are combined when discussing the working principles of the proposed design for the new spectrometer.
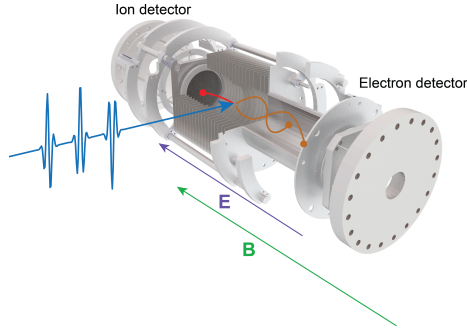
1.2.1 Double time-of-flight spectrometer

Figure 1: A 3D rendering of a double time-of-flight spectrometer, adapted from [6]. Incoming light, marked in blue, enters the spectrometer and ionizes an atom. The electrons are separated from the ion by the electric field, which accelerates the particles in opposite directions. The electrons, here seen as orange trajectories, follow a helical path and complete several periods before impacting the detector screen. This cyclotron motion is induced by the magnetic field. The ion, seen in red, follows a path that is only slightly curved.

Modern time-of-flight spectrometers can measure the initial 3D momentum of all charged particles after an ionization event by recording the impact coordinates on detectors and measuring the time it took to reach the detector, the time of flight. One example, built in-house at the department of physics [7], is presented in figure 1. The electron trajectories are contained within the detector by a cyclotron motion induced by the magnetic field, preventing the electrons from colliding with the spectrometer wall. The ion also follows a helical trajectory but due to its heavy mass the cyclotron period is longer. As such, the ion does not have time to complete a single full revolution before coming to a stop.

The spectrometer is in a vacuum chamber containing two detectors, consisting of a microchannel plate and a delay-line detector each, and a set of electrodes that apply a weak homogeneous electric field along the principal axis of the spectrometer, with a typical strength of $\leq 1000\,\mathrm{V/m}$. The electric field is used to separate particles according to their charge. If the field persists throughout the spectrometer, it is known as a single-field configuration. If the field instead terminates at some point before the detectors, it is known as a two-field configuration, where the field-free region is denoted as the drift tube. The length of the active region and the drift tube can be chosen such that a time-focusing condition is fulfilled [8]. For the purposes of this project, only the single-field configuration is considered. In addition to the electric field some devices, such as the one in Lund, also employ a homogeneous magnetic field in order to radially confine the particles in a cyclotron motion.

While in operation, a pulsed light source will intersect an atomic or molecular beam. When the particles are ionized the dissociation products interact with the external fields via the Lorentz force:

$$\mathbf{F}_L = q\mathbf{E} + q\mathbf{v} \times \mathbf{B}. \tag{1}$$

Here it is useful to define the cyclotron radius as:

$$R = \frac{mv_t}{|q|B}. \tag{2}$$

where m is the mass of the charged particle, q its charge and v_t its transverse velocity with respect to the magnetic field. For the interested reader, the solutions to the equations of motion are given in appendix A.1 When a charged particle eventually reaches a detector it strikes microchannel plates which sets of an electron cascade that is projected onto a delay-line detector behind the microchannel plates. The delay-line detector then records the impact coordinates of the particle. With each laser pulse, a start signal is sent to a time-to-digital converter and when a particle reaches the detector, the microchannel plates provide the stop signal; it is in this manner that the time of flight is measured. With these data points in hand, that is the impact position and the time of flight, it is then possible to calculate all components of the initial momentum.

1.2.2 The Stern-Gerlach apparatus

The Stern-Gerlach device is, like the time-of-flight spectrometer, situated inside an evacuated chamber with an injection port in one end, a detector in the other and a pair of magnets between these. I diagram of the setup can be found in figure 2. When in use, a particle beam of neutral particles is shot in through the port and pass through a gap between the magnets, finally impacting the detector on the other side. Since the particles are neutral, the only force acting on them will be due to the interaction between their dipole moments and the magnetic field gradient. It was in this way Stern and Gerlach first showed the quantization of the magnetic moment of silver atoms [9].
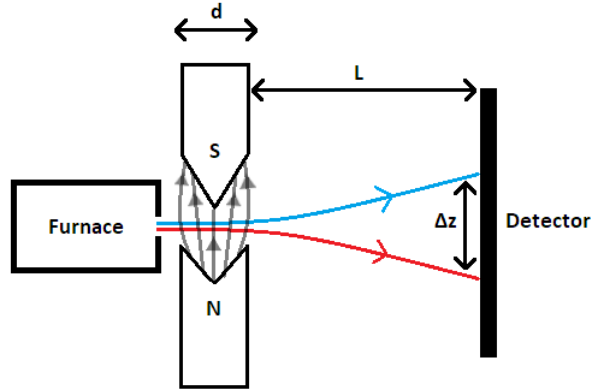

Figure 2: Simple diagram of a Stern-Gerlach device. The two magnets, labeled as north and south, produce an inhomogeneous magnetic field in the region between them marked by the transparent gray field lines. This deflects the trajectories of the neutral particles that are ejected from the furnace. The turqoise curve represents the trajectory of a particle with spin up with respect to the magnetic field while the red curve represents a particle with spin down. The particles interact with the field gradient as they pass through region d and then drift in the region L before impacting the detector, producing a spin separation Δz.

It is well-known that inside a homogeneous external field, a magnetic dipole may experience a torque but never a net force. Once a field gradient is introduced, however, this changes. Here the *magnetic field gradient* refers to the gradient of the scalar product of the magnetic moment and the magnetic field divided by the magnitude of the magnetic moment. That is

$$\frac{1}{|\boldsymbol{\mu}|}\nabla(\boldsymbol{\mu}\cdot\mathbf{B}) = \frac{1}{\mu}\nabla(\mu B\cos\theta) = \nabla B\cos\theta. \tag{3}$$

Here $\boldsymbol{\mu}$ is the magnetic moment of the particle, $\mathbf{B}$ is the magnetic field and θ is the angle between them. The force on a magnetic dipole in an inhomogeneous external field takes the following form:

$$\mathbf{F}_{SG} = \nabla\left(\boldsymbol{\mu}\cdot\mathbf{B}\right). \tag{4}$$

It is this force that is utilized in a Stern-Gerlach device in order to separate particles according to their spins. Perhaps the most obvious example of this force is when two ordinary bar magnets attract one another. Interestingly this expression holds for quantum particles as well, though, in this case the direction and magnitude of the magnetic moment are both quantized.

1.3 The Stern-Gerlach spectrometer for charged particles

Now the principles of measurement of charged particles in (E,B) fields and techniques for how spin can be measured have been reviewed. This project proposes to study the motion of charged particles in the presence of an inhomogeneous magnetic field. The inhomogeniety of the field produce a difference between the case where the particle has a spin up (parallel to the magnetic field) and when the spin is down (antiparallel to the magnetic field), given otherwise identical initial conditions, similarly to the

Stern-Gerlach experiment. In this work, only particles with a magnetic moment such that $\boldsymbol{\mu} = (0, 0, \pm\mu)$ are considered.

The conceptual setup that was studied is depicted in figure 3, where the motion of an ion in a magnetic and electric field is illustrated. A simple coil is used to adjust the parameter of the magnetic field. The purpose of this setup is not to precisely measure natural constants, such as the Bohr magneton, but rather to investigate spin in dynamic situations while simultaneously recording the kinematics of the particle. The plan is to extract and measure particles in the same manner as the time-of-flight spectrometer. Due to time constraints only a simplified setup with a single-field time-of-flight spectrometer is considered.
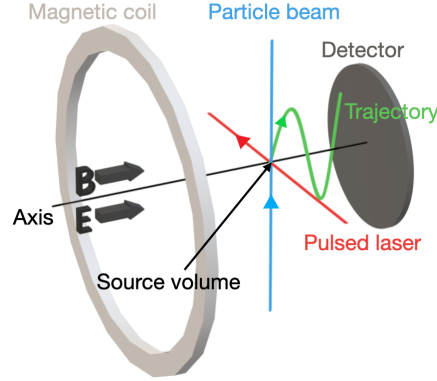

Figure 3: Schematics of the proposed setup to measure the spin of a positively charged particle. The turquoise particle beam, with a velocity $\mathbf{v_0}$, intersects with the red pulsed laser that produces an ion. The ion then moves along the green, helical trajectory until it reaches the gray detector plate. The white ring denotes the coil which produces a strong inhomegenous magnetic field. Both magnetic and electric fields are aligned along the spectrometer axis which is denoted by the black line.

Let the electric and magnetic fields take the following forms in Cartesian coordinates:

$$\mathbf{E} = (0, 0, E), \qquad \mathbf{B} = (0, 0, B), \qquad B = B\left(z(t)\right), \tag{5}$$

with a gradient

$$\nabla\left(\boldsymbol{\mu} \cdot \mathbf{B}\right) = \mu \nabla B \cos\theta = \mu \frac{\mathrm{d}B}{\mathrm{d}z} \cos\theta\, \hat{\mathbf{z}}. \tag{6}$$

In reality it can be difficult to construct such a magnetic field; the magnetic field gradient necessarily has components in two, or more, Cartesian directions. However, assuming a coil to be infinitely large with respect to the cyclotron radius this approximation should be satisfied, providing the essential results regarding the spin separation in space. The other components of the gradient would complicate the transverse equations of motion but it would not impact the longitudinal motion or the spin separation. In this context, given these fields and a magnetic moment such that $\theta = 0$ or $\theta = \pi$, the force on some particle becomes

$$\mathbf{F}_{\text{tot}} = \mathbf{F}_B + \mathbf{F}_E + \mathbf{F}_\mu = qv_yB\,\hat{\mathbf{x}} - qv_xB\,\hat{\mathbf{y}} + \left(qE \pm \mu\frac{\mathrm{d}B}{\mathrm{d}z}\right)\hat{\mathbf{z}}. \tag{7}$$

The total force, $\mathbf{F}_{\text{tot}}$, constitutes of the Lorentz force, $\mathbf{F}_B + \mathbf{F}_E$, and the Stern-Gerlach force, here denoted $\mathbf{F}_\mu$. m and q are the mass and charge of the particle respectively. From this, the equations of motion can be formulated:

$$\dot{v}_x = \frac{q}{m}v_yB, \qquad \dot{v}_y = -\frac{q}{m}v_xB, \qquad \dot{v}_z = \frac{qE}{m} \pm \frac{\mu}{m}\frac{\mathrm{d}B}{\mathrm{d}z}. \tag{8}$$

Here v_i are the Cartesian components of the velocity of the particle. No obvious analytical solutions were found (see appendix A.2), but it is possible to numerically integrate these equations, which is in essence all that is needed for this project. One difficulty with this approach, however, is that the Stern-Gerlach force is around five orders of magnitude smaller than the Lorentz force and, as such, high precision is

required for the numerical approach to work. In order to be considered successful, the simulations would need to produce an observable spin separation between spin up/down cases given reasonable parameters.

As mentioned earlier, a simple coil made circular loop of current is used to produce a magnetic field. On the symmetry axis of the coil, the magnetic field takes the following form:

$$\mathbf{B} = \frac{\mu_0 I}{2} \frac{R^2}{(R^2 + z^2)^{3/2}} \hat{\mathbf{z}} = \frac{B_0 R^3}{(R^2 + z^2)^{3/2}} \hat{\mathbf{z}}. \tag{9}$$

where I is the current through the loop, R is the radius of the loop, B_0 is the magnetic field strength at the center of the loop and z is the height at which the field is being evaluated. Furthermore, μ_0 is the permeability of free space. As soon as there is some transverse deviation, call it ε, from the z-axis, the expression in equation (9) should be corrected [10]. However, as long as $\varepsilon \ll R$, this can still be used as an approximation. To artificially increase the magnetic field gradient, it is worth considering a more general expression as well:

$$\mathbf{B} = \frac{B_0 R^{2\lambda}}{(R^2 + z^2)^{\lambda}} \hat{\mathbf{z}}. \tag{10}$$

In this project, the primary focus lies on the simple coil design, although, the impact of varying λ is also considered.

Finally, another approximation done was in regards to the size of the source volume, i.e. the region of intersection between the particle beam and the laser. The size of the volume was neglected, that is, it was regarded as point-like. However, in reality this intersection will span some finite volume. In practice, the finite extension of the source volume will cause a blurring effect in the detector readout.

1.4   This work

As many factors can influence the final realization of an instrument measuring the spin of electron and ions simultaneously, the numerical simulation created for this project considers an idealized system described in 1.3 to address two objectives:

- Find conditions where a $1\,\mathrm{mm}$ spin separation can be achieved. This limit is set by the typical size of a source volume for the particles which should be $\leq 1\,\mathrm{mm}^3$. If the spin separation is less than this, it will be obscured by the blurring effect caused by the source volume.

- Identify the (E,B) field configurations that produce well-behaved trajectories that can easily be measured. This objective is essential for any practical realization of the device as it enables the installation of a microchannel plate and a delay-line detector with a suitable geometry.

Aside from these objectives, a set of limitations is imposed:

- The trajectory should not span more than one meter along the spectrometer axis (the z-direction) as to not make the device overly large;

- The magnetic field strength should not exceed $1\,\mathrm{T}$, which can be achieved with regular electromagnet at room temperature;

- The electric field used to extract particles should be $\leq 1000\,\mathrm{V/m}$ in order to measure both electrons and ions simultaneously.

These objectives and limitations set the boundary of what is to be considered the *practical regime.* This regime is of importance as it would be difficult to build and operate a device beyond these conditions. Of all these conditions, the most strict is that of the spin separation. Furthermore, another important requirement for the project is that the repetition rate of the pulsed light source should be inversely proportional to the time of flight or lower as to allow for consecutive measurements. This condition will define the practical regime where an experiment measuring electron and ions simultaneously can be performed with the light source available at the department of physics in Lund. The sought solutions are those where the time of flight do not exceed $10\,\mu\mathrm{s}$.

2 Method

In this section an outline of the simulation is presented, followed by a description of the adjustable settings. The full code listing is detailed in appendix B. Lastly, the numerical convergence is discussed.

2.1 Simulation

The program for the simulation has been written in the programming language Python. The simulation takes the known acceleration of the particle and numerically integrates it two times in order to calculate the final position of the particle. The simulation runs for both the spin up and spin down case simultaneously such that the two cases may be compared side by side. What follows is a description of how the simulation works.

The simulation employs a modified fourth order Runge-Kutta method. The Runge-Kutta had to be modified from its classical version since the dependent variable (that is time) is absent from all equations of motion and the equation for z is a second order equation rather than a first order one. Before the method is presented in full, however, an argument is made for why the magnetic field and its gradient can be considered as constant throughout one step. For simplicity, consider a case when the electric field is set to zero such that, according to equation (8),

$$\dot{v}_z = \frac{\beta z}{(R^2 + z^2)^{\lambda+1}}.\tag{11}$$

The first Runge-Kutta coefficient for z then is

$$k_{1z} = \frac{\beta z}{(R^2 + z^2)^{\lambda+1}}\, \mathrm{d}t.\tag{12}$$

The second coefficient becomes

$$k_{2z} = \frac{\beta(z + k_{1z}\, \mathrm{d}t)}{\left(R^2 + (z + k_{1z}\, \mathrm{d}t)^2\right)^{\lambda+1}}\, \mathrm{d}t.\tag{13}$$

A typical time step in these simulations is on the order of nanoseconds or lower and, as such, all the coefficients for z can be approximated to be the same:

$$\mathrm{d}t^2 = 10^{-18}\, \mathrm{s}^2 \Rightarrow k_{1z}\, \mathrm{d}t \approx 0 \Rightarrow k_{1z} \approx k_{nz}, \quad n = 2, 3, 4.\tag{14}$$

Furthermore, the impact on the transverse components is also negligible; take $\dot{v}_{x2}$ as an example:

$$\dot{v}_{x2} = \kappa \left(v_y + \frac{k_{y1}}{2}\right) \frac{1}{\left(R^2 + \left(z + \frac{k_{z1}\, \mathrm{d}t}{2}\right)^2\right)^{\lambda}} \approx \kappa \left(v_y + \frac{k_{y1}}{2}\right) \frac{1}{(R^2 + z^2)^{\lambda}}.\tag{15}$$

The contribution from the z-coefficients is vanishingly small, hence magnetic field and its gradient are considered as constant during one Runge-Kutta step. With this in mind, the procedure takes the following form:

$$\dot{v}_{x1} = \alpha v_y,\tag{16}$$

$$\dot{v}_{y2} = -\alpha v_x,\tag{17}$$

$$\dot{v}_z = \gamma \pm \frac{\mu}{m}\frac{\mathrm{d}B}{\mathrm{d}z} \Rightarrow\tag{18}$$

$$k_{x1} = \dot{v}_x\, \mathrm{d}t,\tag{19}$$

$$k_{y1} = \dot{v}_y\, \mathrm{d}t,\tag{20}$$

$$k_z = \dot{v}_z\, \mathrm{d}t.\tag{21}$$

With the first order coefficients a new acceleration is found:

$$\dot{v}_{x2} = \alpha \left(v_y + \frac{k_{y1}}{2} \right), \tag{22}$$

$$\dot{v}_{y2} = -\alpha \left(v_x + \frac{k_{x1}}{2} \right), \tag{23}$$

$$k_{x2} = \dot{v}_{x2} \, \mathrm{d}t, \tag{24}$$
$$k_{y2} = \dot{v}_{y2} \, \mathrm{d}t. \tag{25}$$

Repeating the same procedure to find the third order coefficients:

$$\dot{v}_{x3} = \alpha \left(v_y + \frac{k_{y2}}{2} \right), \tag{26}$$

$$\dot{v}_{y3} = -\alpha \left(v_x + \frac{k_{x2}}{2} \right), \tag{27}$$

$$k_{x3} = \dot{v}_{x3} \, \mathrm{d}t, \tag{28}$$
$$k_{y3} = \dot{v}_{y3} \, \mathrm{d}t. \tag{29}$$

Lastly, the fourth order coefficients are computed with a slight difference to the previous two steps:

$$\dot{v}_{x4} = \alpha \left(v_y + k_{y3} \right), \tag{30}$$

$$\dot{v}_{y4} = -\alpha \left(v_x + k_{x3} \right), \tag{31}$$

$$k_{x4} = \dot{v}_{x4} \, \mathrm{d}t, \tag{32}$$
$$k_{y4} = \dot{v}_{y4} \, \mathrm{d}t. \tag{33}$$

Now, finally, the new velocity can be computed:

$$v_{x\mathrm{new}} = v_x + \frac{k_{x1} + 2k_{x2} + 2k_{x3} + k_{x4}}{6}, \tag{34}$$

$$v_{y\mathrm{new}} = v_y + \frac{k_{y1} + 2k_{y2} + 2k_{y3} + k_{y4}}{6}, \tag{35}$$

$$v_{z\mathrm{new}} = v_z + k_z, \tag{36}$$

$$\mathbf{v}_{\mathrm{new}} = (v_{x\mathrm{new}}, v_{y\mathrm{new}}, v_{z\mathrm{new}}). \tag{37}$$

The new position is then calculated with an ordinary Euler step:

$$\mathbf{r}_{\mathrm{new}} = \mathbf{r}_{\mathrm{old}} + \mathbf{v}_{\mathrm{new}} \, \mathrm{d}t. \tag{38}$$

The reason why the new position is calculated using an Euler step, rather than another Runge-Kutta step, is due to the fact that the velocity is not explicitly known. It is a requirement that the derivative is known when using the Runge-Kutta method, hence it is not used in this last step. This constitutes the core process of the simulation. In addition to this, several other methods are implemented to record and monitor different aspects of the particle motion.

Worth noting is the fact that no matter where in the xy-plane the particle finds itself, the expression for the magnetic field does not change; the particle is always treated as if it is on the z-axis by the field. This simplification ignores the transverse components of the magnetic field, and so the trajectories for large cyclotron radii will not be accurately represented. Importantly, however, this does not affect the spin separation. Furthermore, this can be remedied by a larger loop radius with a larger current running through it, as to decrease the relative deviation from the z-axis while keeping the magnetic field strength constant.

2.2 Settings

The simulation has several settings that can be adjusted freely, both for the particles, the detector and the simulation itself. The available spectrometer settings are:

- Electric field strength,

- Magnetic field strength,

- Coil radius,

- Falloff exponent.

For all simulations, the loop radius is held fixed at $1\,\mathrm{m}$. The settings for the particle are:

- Mass, which was held at four proton masses or one electron mass.

- Charge, held at one positive or negative elementary charge.

- Magnetic moment, set as one negative Bohr magneton [11].

- Initial transverse kinetic energy along the x-axis. The particle always started out with an energy perfectly collimated along the x-direction.

- Starting position along the z-axis.

For the ions, two different cases are considered for the kinetic energy: the thermal case, where the ions have an energy of $25\,\mathrm{meV}$ and the high-energy case, where their kinetic energy is $3\,\mathrm{keV}$. Electrons can, in principle, have a distribution of kinetic energy, E_k, according to

$$E_k \leq h\nu - V_{\mathrm{IP}}, \tag{39}$$

where $h\nu$ is the photon energy, and V_{IP} is the ionization potential of the atom [12]. For sake of simplicity, the kinetic energy of the electron was set to 10 eV.

The primary settings for the simulation are the time of flight and the recording parameter. When plotting the trajectory, the position of the particle is recorded at regular intervals; the size of these intervals is controlled by the recording parameter. The reason for not recording and plotting the position of every time step is in order to limit the run time and to make the graphs easier to view.

2.3 Numerical convergence

2.3.1 Ions

Although the transverse components of the particle motion takes advantage of a Runge-Kutta method, the longitudinal component uses a simple Euler method. The numerical convergence of the spin separation can be seen in figure 4 and figure 5 for high energy ions and thermal ions respectively.
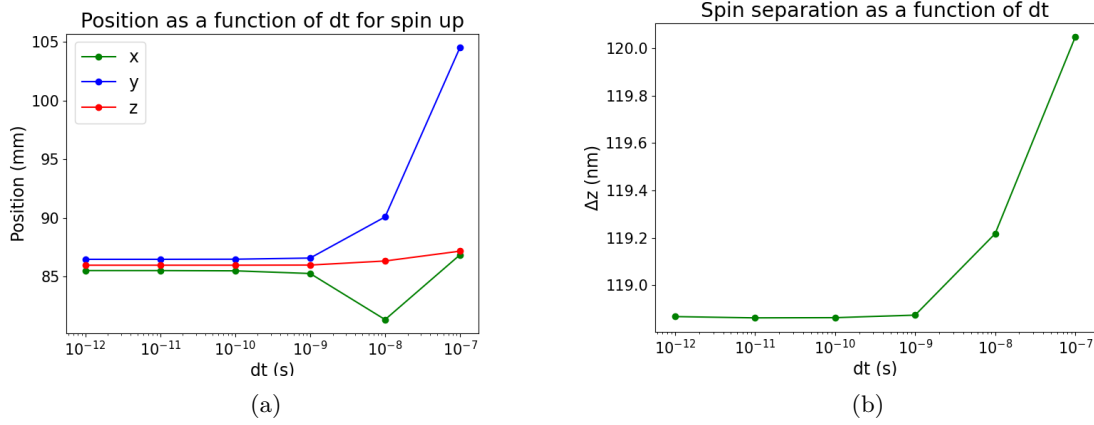
(a) (b)

Figure 4: Shown to the right is the numerical convergence of the position for high energy ions. The case shown is for spin up, although the plot for spin down is identical. All three dimensions seem to stabilize at $dt = 10^{-10}$. The location of all three curves have been adjusted in order to make them easier to view and compare. To the left the convergence of the spin separation can be seen. Note that the graph is adjusted slightly upwards for $dt = 10^{-12}$, something that is barely visible in the graph. For this simulation, the magnetic field is $B_0 = 1\,T$, the electric field is $E = 100\,V/m$, the initial kinetic energy is $3\,keV$, the starting height is $z_0 = 48\,cm$, the falloff exponent is $\lambda = 3/2$ and the time of flight is $10\,\mu s$.
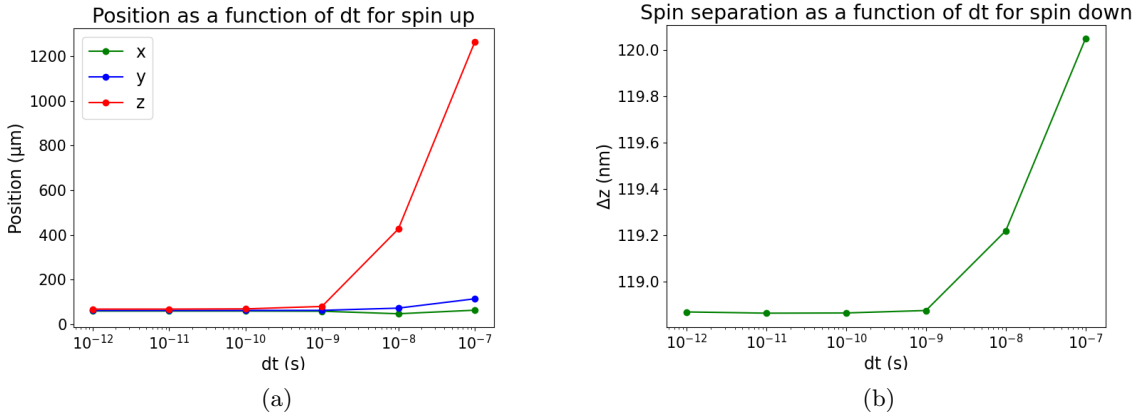

(a) (b)

Figure 5: The numerical convergence for thermal ions. The settings, a part from the kinetic energy, are identical to that of the high energy case. As can be seen, there is no change in the behaviour of the longitudinal motion as the convergence of both the spin separation and the z-position looks identical to the high energy case. The transverse components, however, are now smaller. Once more, all components along with the spin separation seem to converge well beyond $dt = 10^{-10}$.

2.3.2 Electrons

The electron case is somewhat more intricate than that for ions; in an ionization event, due to the comparatively heavy mass of ions, the momentum is largely unaffected and the ion continues along its original path. In contrast, electrons do not generally stay true to the path of the atom after ionization. Rather, they may fly off in any direction and, as such, it cannot be assumed that they remain collimated after the event. For this reason, all the components of the velocity become relevant to the subsequent behaviour of the electron. Even though the position seem well-behaved for $dt \leq 10^{-12}$, this is contradicted by the lack of convergence for the spin separation as seen in figure 6.
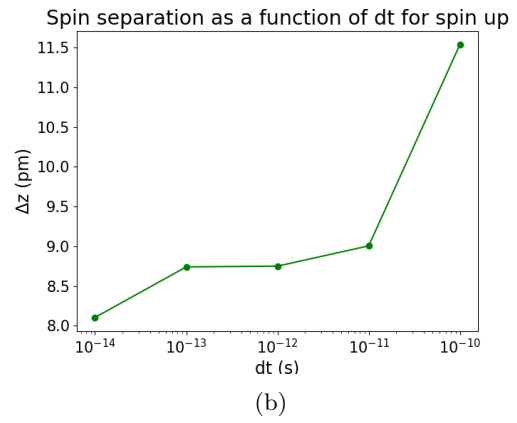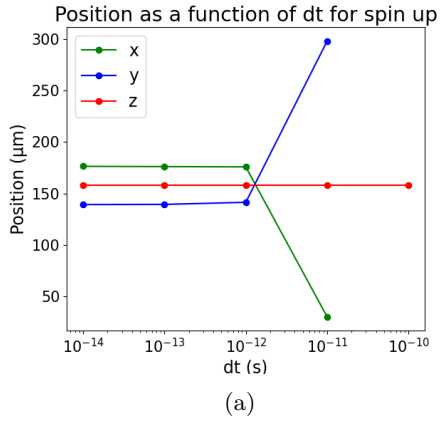
Figure 6: To the left, the numerical convergence of the position for electrons is shown. The curves have been adjusted along the vertical axis for a better view. Notably, the points at $\mathrm{d}t = 10^{-10}$ are missing for x and y. This is because they diverged to a value $> 10^{30}\,\mathrm{m}$ and so they could not be viewed in the same graph. To the right, the convergence of the spin separation is shown. It does not converge. As for the settings, the magnetic field is $1\,\mathrm{T}$, the electric field is off, the initial kinetic energy is $10\,\mathrm{eV}$, the starting height is $50\,\mathrm{cm}$, the falloff exponent is $3/2$ and the time of flight is $1\,\mathrm{ns}$.

3 Results

In this section, a set of typical ion trajectories are presented at first as to give a sense of how the simulation behaves. After this, the impact of varying different settings is shown for ions. Lastly, the electron case is discussed.

3.1 Ions

To start with, typical trajectories of helium atoms for different time-of-flights and electrical fields are illustrated. These trajectories are summarized in the figures in table 1, where the trajectory for spin up is shown in blue, and spin down is shown in red. One important thing to note is that when the electric field is turned on, the spin up path is almost not visible; because the spin up trajectory nearly coincides with the spin down trajectory, it becomes hard to see on the scale of the figures.

Table 1: Some typical ion trajectories with the electric field on and off. Except for the electric field and time of flight the settings for all these simulations are the same, and they are as follows: The kinetic energy is $3\,\text{keV}$, initially perfectly collimated along the x-axis; the maximum magnetic field strength is $B_0 = 1\,\text{T}$ at the center of the current loop; the falloff exponent is set $3/2$; and the particle starts of at $z_0 = 50\,\text{cm}$ above the plane of the loop. The electric and magnetic fields are always directed upwards, along the z-axis.
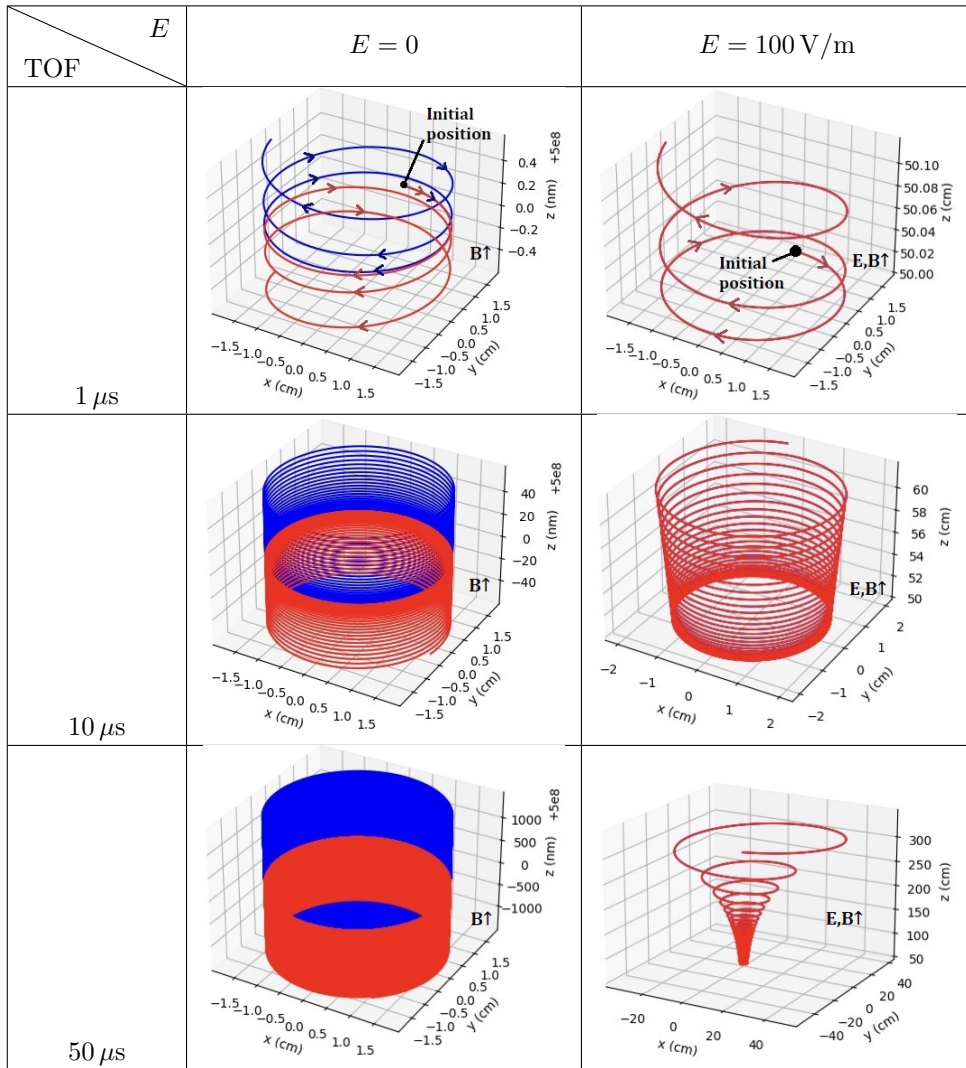
When the electric field is off the trajectories retain the shape of a circular helix. Ions with different spins are spatially separated: spin up moves upward while the spin down moves downward. As the time of flight increases, the separation increases as seen by the longitudinal scale which is larger but remains below 1 μm. Under this condition, when the change in height is small, the B-field is essentially constant, making the change in Larmor radius indistinguishable. Furthermore, the gaps between the cyclotron laps appear progressively smaller, and finally, the trajectory looks like a solid shape when the time of flight reaches 50 μs.

When the electric field is on, even for the shortest time of flight, that is 1 μs, the trajectory takes on macroscopic proportions in order of 1 mm. As previously stated, the spin separation is too small to be seen on this scale. The helical trajectory as a whole looks similar to its counter part where the electric field is off, meaning that the change in the magnetic field has no noticeable effect on the Larmor radius. Increasing the time of flight to 10 μs, the change in radius is now visible and it appears linear. In regards to the practicality, this would be close to an ideal trajectory shape; the height is shorter than one meter, it has a macroscopic radius and the gap between the cyclotron periods is reasonably wide. However, the spin separation is around four orders of magnitude smaller than the target value of 1 mm. When the time of flight is 50 μs, the trajectory is becoming increasingly loosely bound. Notably, the particle ends up several meters above its starting point. At this scale it is clear that the increase in radius is not linear.

For all of these trajectories the spin separation never exceeds 10 μm, which is two orders of magnitude smaller than the target separation of 1 mm. It seems that, on the face of it, the objective is not achievable with ions within a few tens of μs. In the following, the separation between particles of different spins as a function of different settings is qualitatively investigated.

3.1.1 Time of Flight

The results of the simulations for high energy ions are reported in figure 7. The values for thermal ions are identical and thus it can be inferred that the transverse energy of the ions have no impact on the spin separation. This spin separation increases non-linearly for a short time of flight, as seen in figure 7 (a), whether or not the electric field is on. However when the time of flight is longer, as in figure 7 (b), as soon as the electric field is enabled the spin separation takes on a linear behaviour. This can be explained as the particle becoming unbound by the magnetic field such that the spin trajectories are linearly drifting apart. In other words, the gradient of the B-field is negligible. It was found that the spin separation reaches upwards of 10 μm.
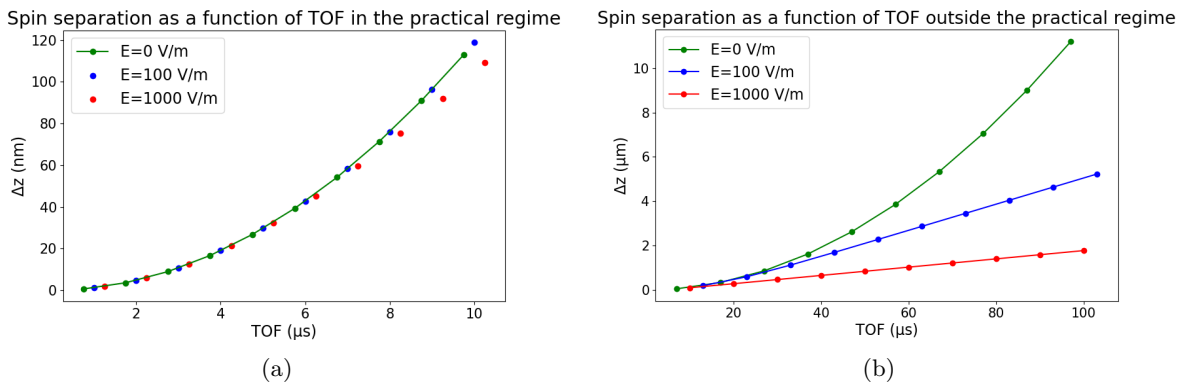
Figure 7: The affect of a varying time of flight. In (a), for shorter times of flight, the trajectories remain largely unaffected by the electric field strength. In (b), for longer times of flight, the presence of an electric field has a noticeable impact on the spin separation. Note that the two graphs have different vertical scales: In (a) the separation is measured in nanometers, in (b) the separation reaches the order of micrometers. The maximum magnetic field strength is $B_0 = 1$ T, the starting height is at $z_0 = 48$ cm, the falloff exponent is $\lambda = 3/2$ and the time step size is d$t = 10^{-10}$ s.

3.1.2 Starting position along the z-axis

During this study, it was found that the electrical field had an influence on the optimal initial position along the z-axis. The spin separation as a function of the starting position is shown in figure 8. When the electric field is off, the optimal point for the particle to start at is at $(0, 0, 0.5)$, represented by the green curve. As shown in appendix A.3, the Stern-Gerlach force reaches its maximum at

$$z = \frac{1}{\sqrt{1 + 2\lambda}}, \tag{40}$$

which means that $z = 50\,\text{cm}$ when $\lambda = 3/2$. Since the particle is basically stationary when the electric field is off, the optimal starting height is where the force is strongest.

In contrast, when the electric field is on the particle will quickly move through the region where the force is strong and, as such, a downward offset in the starting position is required to optimize the spin separation. This offset preempts the movement due to the electric field and maximizes the time spent where the Stern-Gerlach force is strong.
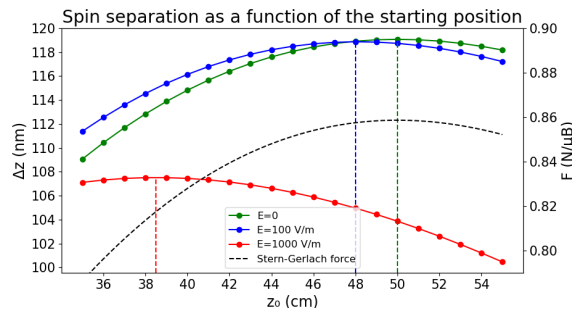

Figure 8: When the electric field is off the maximum separation is achieved at $z_0 = 50\,\text{cm}$ where the Stern-Gerlach force is the strongest. When $E = 100\,\text{V/m}$ the optimal offset is $2\,\text{cm}$ downward and the maximum separation less than $1\,\text{nm}$ smaller than when the field is zero. When $E = 1000\,\text{V/m}$ the optimal offset is between $11 - 12\,\text{cm}$ down and the separation is visibly lower. The maximum magnetic field strength is $B_0 = 1\,\text{T}$, the falloff exponent is $\lambda = 3/2$, the time step size is $dt = 10^{-11}\,\text{s}$ and the time of flight it set to be $10\,\mu\text{s}$. The black curve shows the Stern-Gerlach force for reference. As seen in the scale to the right, the force is given in units of Newtons per Bohr magneton. The maximum separations have been marked by vertical dashed lines in the same color as the graph they belong to.

3.1.3 Magnetic field strength

The spin separation as a function of the magnetic field strength is presented in figure 9 below. It follows a linear trend, though, for a high electric field the slope is diminished.
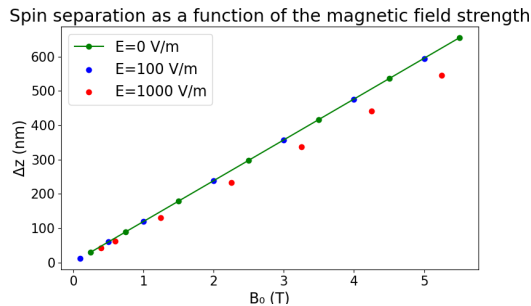

Figure 9: The spin separation depends linearly on the magnetic field strength. The electric field is off, the starting height is $z_0 = 50\,\text{cm}$, the falloff exponent is $\lambda = 3/2$, the time step size is $dt = 10^{-11}\,\text{s}$ and the time of flight it set to be $10\,\mu\text{s}$.

3.1.4 Falloff exponent

When considering the case of a field gradient generated via a simple loop current, it may also be worth exploring similar cases. In this subsection a magnetic field of the form seen in equation (10) is examined. For the falloff exponent λ, as outlined in appendix A, the optimal value in terms of spin separation when $R = 1$ is

$$\lambda = \ln^{-1}\left(1 + z^2\right). \tag{41}$$

In the case where $z = 50\,\text{cm}$ this becomes $\lambda \approx 4.48$. Setting $\lambda = 4.48$ increases the force one and a half times compared to the current loop, where $\lambda = 3/2$. As seen in figure 10, the simulations agree with the theoretical result. This shows that, for something similar to a loop current, it is not possible to increase the spin separation indefinitely by increasing the falloff exponent.
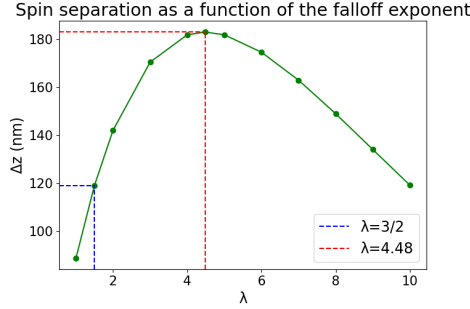

Figure 10: The spin separation increases from just below $120\,\text{nm}$ to $183\,\text{nm}$ as λ moves from $3/2$ to its optimal value around 4.48. The maximum magnetic field strength is $B_0 = 1\,\text{T}$, the electric field is off, the starting height is $z_0 = 48\,\text{cm}$, the kinetic energy is $3\,\text{keV}$, the time of flight is held at $10\,\mu s$ and the time step size is $dt = 10^{-11}\,\text{s}$.

3.2 Electrons

Electrons are several thousand times lighter than ions, and so it seems plausible that the smaller mass may make it possible to reach the target separation. However, the smaller mass means that the Larmor radius becomes smaller as well, meaning sharper turns and a need for increased numerical precision. So much so that the required step size becomes too small for Python. An illustration of the problem is found in figure 11.

(a) $dt = 10\,\text{ps}$ (b) $dt = 1\,\text{ps}$ (c) $dt = 0.1\,\text{ps}$
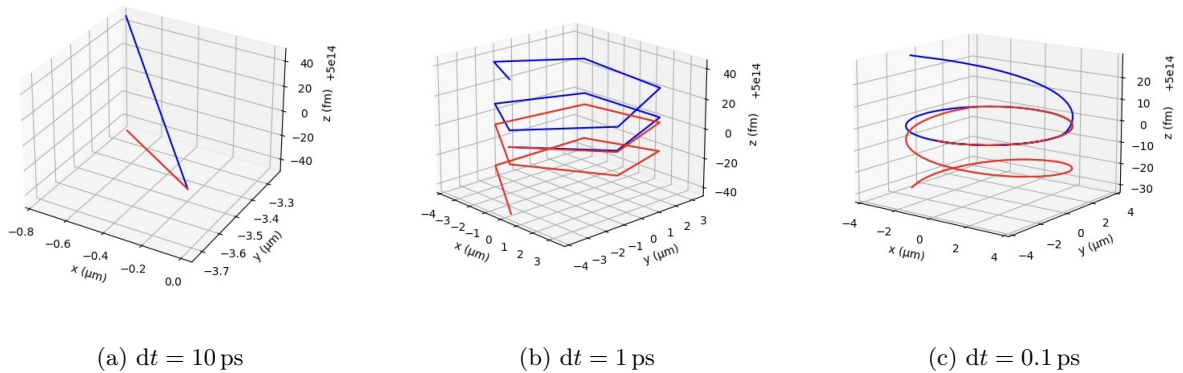
Figure 11: The simulation for electrons with increasingly small time steps. The time of flight is limited to $0.1\,\text{ns}$, the magnetic field strength is $B_0 = 1\,\text{T}$, the electric field is off, the starting height is $z_0 = 50\,\text{cm}$, the kinetic energy is $10\,\text{eV}$ and the falloff exponent is $\lambda = 3/2$. In the first case, the simulation simply breaks. In the second case trajectory is generated, although the radial motion is jagged. The last trajectory looks smooth, but the movement in the longitudinal direction is no longer accurately simulated.

For the first trajectory in figure 11, the time steps is clearly too large, as well as in the second one. At first glance, the third one looks smooth and so should produce an accurate result in the full scale. On closer inspection, however, it is seen that the spin separation is zero for the first part of the simulation after which there is a sharp onset. Furthermore, there seems to be an asymmetry between spin up and down. Inspecting the longitudinal step size dz reveals that it is too small for Python; the steps are simply truncated to zero for the first part of the simulation until they reach a threshold value and are suddenly no longer neglected. This might explain the lack of numerical convergence, but prohibitively long run times prevents further investigation.

4   Discussion

Our results show that it is not possible to reach the target separation for ions within the sought practical regime. The spin separation within the practical regime is generally around $\sim 100\,\text{nm}$. In order to meet the set target of $1\,\text{mm}$ it needs to increase by four orders of magnitude, something which is not possible even if the starting position and the falloff exponent are optimized since this does not significantly boost separation. Full scale simulations show that it takes the ion $916\,\mu\text{s}$, just under $1\,\text{ms}$, to reach a $1\,\text{mm}$ separation while otherwise staying within the practical regime. The settings in this case are: $B_0 = 1\,\text{T}$, $E = 0$, $z_0 = 0.5\,\text{m}$ and $\lambda = 3/2$. In order to achieve the separation target, either the gradient or the time of flight would have to increase. In figure 12 the required time of flight required for a $1\,\text{mm}$ separation for a specific field gradient can be seen, along with the upper limit on the repetition rate of the light source.
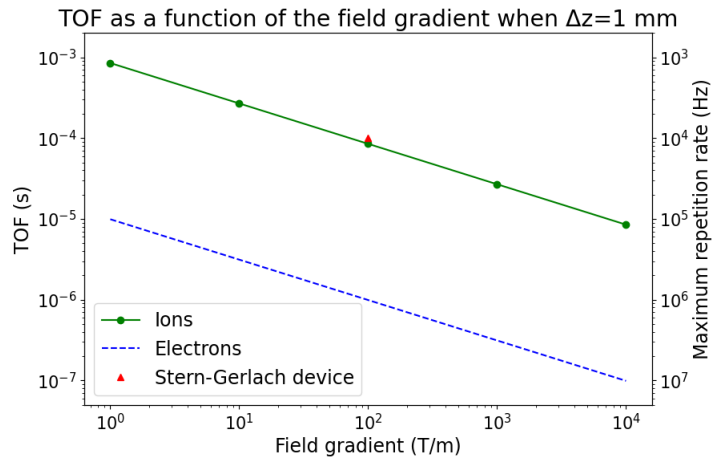
Figure 12: Log-log scaled graph of the time of flight as a function of the field gradient when the spin separation is held fixed at $1\,\text{mm}$. The green line represents ions, the blue dashed line represents electrons and the red triangle denotes the Stern-Gerlach device available at Fysicum. On the scale to the right, the maximum repetition rate of the light source usable in such an experiment is given. It is inversely proportional to the time of flight, as to allow a particle to fully complete its journey before the next laser pulse is emitted.

The quadratic dependence of Δz as function of the time of flight, T, in Figure 7 suggests that if the force on the particle is constant for the duration of the flight, the spin separation follows the impulse-momentum theorem. Indeed, in this case

$$\mathbf{F}_{SG}\Delta t = m\Delta\mathbf{v}, \tag{42}$$

with

$$\Delta z = (\Delta\mathbf{v} \cdot \hat{\mathbf{z}})\Delta t. \tag{43}$$

It can then be deduced that

$$\Delta z = \frac{\mathbf{F}_{SG} \cdot \hat{\mathbf{z}}}{m}T^2 = \frac{\mu}{m}\frac{\partial B}{\partial z}T^2. \tag{44}$$

18

Assuming that

$$\Delta z = 1\,\text{mm}, \qquad \left|\frac{\partial B}{\partial z}\right| \sim 1, \qquad \left|\frac{\mu}{m}\right| \sim 1000,$$

then

$$T = \sqrt{\Delta z \left(\frac{\mu}{m}\frac{\partial B}{\partial z}\right)^{-1}} = 1\,\text{ms}. \tag{45}$$

This agrees well with full scale simulations when the electric field is off; the particle will not move significantly and the force can be approximated as constant. According to this model, in the case of electrons,

$$\Delta z = 1\,\text{mm}, \qquad \left|\frac{\partial B}{\partial z}\right| \sim 1, \qquad \left|\frac{\mu}{m}\right| \sim 10^7 \Rightarrow T = 10\,\mu\text{s}.$$

This shows that, when doing experiments on electrons, it should indeed be possible to operate within the practical regime using the proposed design. Furthermore, any laser with a repetition rate of $100\,\text{kHz}$, or slower, would be sufficient to carry out the experiment. However, this represents a scenario with ideal conditions; in practice the spread in momentum for the electrons will blur the readout and, as such, a separation $> 1\,\text{mm}$ would likely be necessary.

5 Conclusions and Outlook

For ions, it is clear that a spin separation of $1\,\text{mm}$ cannot be achieved within the practical regime. In order to achieve the goal, the time of flight needs to be in the order of milliseconds or the magnetic field would have to be changed into something other than that of a loop current, such that the field gradient can be increased by several orders of magnitude. Another, less practical, solution is to decrease the size of the source volume and so lower the restriction on the spin separation.

For the electrons, it seems that the lack of numerical convergence is due to the numerical limits of Python; the longitudinal steps are truncated at the beginning of each simulation, which has no noticeable effect on the convergence of the position but does affect the convergence of the spin separation. This should have little impact when the time of flight is greater than $1\,\mu\text{s}$ and so a full-scale simulation should converge, although this could not be confirmed. However, a simple impulse model, validated by the results for ion simulations, reveals that it is possible to achieve the target separation within the practical regime when performing experiments on electrons.

In order to accurately simulate the electron case, the following changes are suggested: The size of the time step $\text{d}t$ should be expressed as a function of, for example, z, t or the cyclotron radius rather than as a constant in order to allocate the precision to the beginning of the simulation, where it is most needed; the units should be rescaled as to avoid numbers that are too small; a different method for numerical integration is needed in order to avoid Euler steps completely; and the program should be converted to `C++` in order to improve performance.

Furthermore, electrons, due to their light mass, cannot be presumed to continue to move along the direction of the particle beam once they have disassociated from the atoms. Instead they will be ejected into the spectrometer at all possible angles. This phenomenon will have a blurring effect on the spectrometer readout, something that further studies will have to grapple with in addition to the issues discussed above.

References

[1] M. Kolbe, P. Lushchyk, Petereit, H. J. Elmers, G. Schönhense, A. Oelsner, C. Tusche and J. Kirschner, "Observation of spin flips with a single trapped proton", Physical Review Letters **107**, 207601 (2011).

[2] V. N. Petrov, M. Landolt, M. S. Galaktionov and B. V. Yushenkov, "A new compact 60 kV mott polarimeter for spin polarized electron spectroscopy", Review of Scientific Instruments **68**, 4385–4389 (1997).

[3] L. S. Brown and G. Gabrielse, "Geonium theory: Physics of a single electron or ion in a Penning trap", Reviews of Modern Physics **58**, 233–311 (1986).

[4] S. Ulmer, C. C. Rodegheri, K. Blaum, H. Kracke, A. Mooser, W. Quint and J. Walz, "Observation of spin flips with a single trapped proton", Physical Review Letters **106**, 253001 (2011).

[5] D. Hanneke, S. Fogwell and G. Gabrielse, "New measurement of the electron magnetic moment and the fine structure constant", Physical Review Letters **100**, 120801 (2008).

[6] S. Mikaelsson, J. Vogelsang, C. Guo, I. Sytcevich, A. L. Viotti, F. Langer, Y. C. Cheng, S. Nandi, W. Jin, A. Olofsson, R. Weissenbilder, J. Mauritsson, A. L'Huillier, M. Gisselbrecht and C. L. Arnold, "A high-repetition rate attosecond light source for time-resolved coincidence spectroscopy", Nanophotonics **10**, 117–128 (2021).

[7] Y. C. Cheng, "Ultrafast photoionization dynamics studied with coincidence momentum imaging spectrometers" (Department of Physics, Lund University, 2016).

[8] W. C. Wiley and I. H. McLaren, "Time-of-flight mass spectrometer with improved resolution", Review of Scientific Instruments **26**, 1150–1157 (1955).

[9] W. Gerlach and O. Stern, "Der experimentelle Nachweis der Richtungsquantelung im Magnetfeld", Z. Physik **9**, 349–352 (1922).

[10] T. Jang, H. J. Ha, Y. K. Seo and S. H. Sohn, "Off-axis magnetic fields of a circular loop and a solenoid for the electromagnetic induction of a magnetic pendulum", Journal of Physics Communications **5**, 10.1088/2399-6528/ac0545 (2021).

[11] *The NIST Reference on Constants, Units, and Uncertainty*, National Institute of Standards and Technology, (2018) https://physics.nist.gov/cgi-bin/cuu/Value?mub (visited on 11/12/2022).

[12] A. Einstein, "Über einen die erzeugung und verwandlung des lichtes betreffenden heuristischen gesichtspunkt", Annalen der Physik **322**, 132–148 (1905).

A Appendix - Theory

In this section two cases are considered. In the first case the magnetic field is constant and in the second case the magnetic field is inhomogeneous. In both cases the initial expressions for the equations of motion are the same. Consider the total force on some particle:

$$\mathbf{F}_{\text{tot}} = \mathbf{F}_B + \mathbf{F}_E + \mathbf{F}_\mu = qv_yB\hat{\mathbf{x}} - qv_xB\hat{\mathbf{y}} + \left(qE \pm \mu\frac{\mathrm{d}B}{\mathrm{d}z}\right)\hat{\mathbf{z}}, \tag{46}$$

where $\mathbf{B} = (0, 0, B)$ with a gradient along the z-direction only and $\mathbf{E} = (0, 0, E)$. In reality, it is impossible to generate a magnetic field gradient along only one Cartesian direction. For the purposes of these calculations, however, the other components have been neglected. Let v_n and $\dot{v}_n$ be the nth component of the velocity and the acceleration respectively. The equations of motion are, in Cartesian coordinates, as follows:

$$\dot{v}_x = \frac{q}{m}v_yB(t), \tag{47}$$

$$\dot{v}_y = -\frac{q}{m}v_xB(t), \tag{48}$$

$$\dot{v}_z = \frac{qE}{m} \pm \frac{\mu}{m}\frac{\mathrm{d}B}{\mathrm{d}z}. \tag{49}$$

For ease of reading, let

$$\alpha = \frac{qB(t)}{m}, \qquad \gamma = \frac{qE}{m}.$$

The equations of motion then become

$$\dot{v}_x = \alpha v_y, \tag{50}$$

$$\dot{v}_y = -\alpha v_x, \tag{51}$$

$$\dot{v}_z = \gamma \pm \frac{\mu}{m}\frac{\mathrm{d}B}{\mathrm{d}z}. \tag{52}$$

A.1 A constant magnetic field

The longitudinal equation, that is the one along the z-direction, can be solved straightforwardly by integration:

$$\frac{\mathrm{d}B}{\mathrm{d}z} = 0 \Rightarrow \dot{v}_z = \gamma \Rightarrow v_z = \gamma t + v_{0z} \Rightarrow z = \frac{\gamma t^2}{2} + v_{0z}t. \tag{53}$$

Here v_{0z} is the initial longitudinal velocity. This can be rearranged to generate an expression for v_{0z} given a known time of flight T and a distance between the source point and the detector L:

$$v_{0z} = \frac{L}{T} - \frac{\gamma T}{2}. \tag{54}$$

As for the transverse components, the time derivative of equation (50) is

$$\ddot{v}_x = \frac{\mathrm{d}}{\mathrm{d}t}\alpha v_y = \alpha\dot{v}_y \Leftrightarrow \dot{v}_y = \frac{\ddot{v}_x}{\alpha}. \tag{55}$$

This expression can now be equated to equation (51):

$$\frac{\ddot{v}_x}{\alpha} = -\alpha v_x \Leftrightarrow \ddot{v}_x = -\alpha^2 v_x \Rightarrow \tag{56}$$

$$v_x = C_1\cos(\alpha t + \phi) + C_2\sin(\alpha t + \phi) \tag{57}$$

With this result in mind, equation (50) can be written as

$$\alpha v_y = \ddot{v}_x = \frac{\mathrm{d}}{\mathrm{d}t}\left(C_1\cos(\alpha t + \phi) + C_2\sin(\alpha t + \phi)\right) = \alpha\left(C_2\cos(\alpha t + \phi) - C_1\sin(\alpha t + \phi)\right) \Rightarrow \tag{58}$$

$$v_y = C_2 \cos(\alpha t + \phi) - C_1 \sin(\alpha t + \phi). \tag{59}$$

In order to find these constants, consider the initial conditions where

$$v_x(t = 0) = v_{0x}, \qquad v_y(t = 0) = v_{0y}.$$

Now equations (50) and (51) become

$$\dot{v}_x(t = 0) = \alpha v_{0y} = \alpha \left(C_2 \cos \phi - C_1 \sin \phi \right), \tag{60}$$
$$\dot{v}_y(t = 0) = -\alpha v_{0x} = -\alpha \left(C_1 \cos \phi + C_2 \sin \phi \right). \tag{61}$$

Starting with equation (60):

$$v_{0y} = C_2 \cos \phi - C_1 \sin \phi \Rightarrow C_2 = v_{0y} \sec \phi + C_1 \tan \phi. \tag{62}$$

Inserting this into equation (61) yields that

$$v_{0x} = C_1 \cos \phi + \left(v_{0y} \sec \phi + C_1 \tan \phi \right) \sin \phi = C_1 \left(\cos \phi + \tan \phi \sin \phi \right) + v_{0y} \tan \phi. \tag{63}$$

There is, as always, a trigonometric trick available to simplify this. Consider the following sleight of hand:

$$\cos \phi + \tan \phi \sin \phi = \sec \phi, \qquad \sec \phi - \sin \phi \tan \phi = \cos \phi. \tag{64}$$

Subsequently,

$$v_{0x} = C_1 \sec \phi + v_{0y} \tan \phi \Leftrightarrow C_1 = v_{0x} \cos \phi - v_{0y} \sin \phi \Rightarrow \tag{65}$$
$$C_2 = v_{0y} \sec \phi + \left(v_{0x} \cos \phi - v_{0y} \sin \phi \right) \tan \phi = v_{0x} \sin \phi + v_{0y} \cos \phi. \tag{66}$$

And so the velocities can be written as

$$v_x = \left(v_{0x} \cos \phi - v_{0y} \sin \phi \right) \cos(\alpha t + \phi) + \left(v_{0x} \sin \phi + v_{0y} \cos \phi \right) \sin(\alpha t + \phi), \tag{67}$$

$$v_y = \left(v_{0x} \sin \phi + v_{0y} \cos \phi \right) \cos(\alpha t + \phi) - \left(v_{0x} \cos \phi - v_{0y} \sin \phi \right) \sin(\alpha t + \phi). \tag{68}$$

Since $\dot{\alpha} = 0$ in this case, the coordinates can be found by direct integration:

$$x = \int v_x \, dt = \int \left(C_1 \cos(\alpha t + \phi) + C_2 \sin(\alpha t + \phi) \right) dt = \tag{69}$$

$$\frac{C_1}{\alpha} \sin(\alpha t + \phi) - \frac{C_2}{\alpha} \cos(\alpha t + \phi) = -\frac{v_y}{\alpha}$$

and, similarly,

$$y = \int v_y \, dt = \int \left(C_2 \cos(\alpha t + \phi) - C_1 \sin(\alpha t + \phi) \right) dt = \tag{70}$$

$$\frac{C_2}{\alpha} \sin(\alpha t + \phi) + \frac{C_1}{\alpha} \cos(\alpha t + \phi) = \frac{v_x}{\alpha}.$$

Note that the integration constants have been scaled away. In conclusion

$$x = -\frac{v_y}{\alpha} = \alpha^{-1} \left(v_{0x} \cos \phi - v_{0y} \sin \phi \right) \sin(\alpha t + \phi) - \alpha^{-1} \left(v_{0x} \sin \phi + v_{0y} \cos \phi \right) \cos(\alpha t + \phi), \tag{71}$$

$$y = \frac{v_x}{\alpha} = \alpha^{-1} \left(v_{0x} \cos \phi - v_{0y} \sin \phi \right) \cos(\alpha t + \phi) + \alpha^{-1} \left(v_{0x} \sin \phi + v_{0y} \cos \phi \right) \sin(\alpha t + \phi). \tag{72}$$

A.2   A variable magnetic field

A.2.1   The longitudinal equation

For ease of reading, let $\dot{v}_z = \ddot{z}$. The equation of motion is

$$\ddot{z} = \frac{qE}{m} \pm \frac{\mu}{m}\frac{\mathrm{d}B}{\mathrm{d}z}. \tag{73}$$

Assuming that the loop radius R is much greater than the Larmor radius r, the eleptical integrals that are otherwise present in the expression for the magnetic field can be neglected:

$$r \ll R \Rightarrow \mathbf{B} \approx \frac{\mu_0 I}{2}\frac{R^2}{(R^2+z^2)^{3/2}}\,\hat{\mathbf{z}} = B_0\frac{R^3}{(R^2+z^2)^{3/2}}\,\hat{\mathbf{z}}. \tag{74}$$

It is possible to modify the shape of this field, for example by adding more closely packed loops. In order to encapsulate these situations in this calculation, consider a more general form of the field:

$$\mathbf{B} \approx \frac{B_0 R^{2\lambda}}{(R^2+z^2)^{\lambda}}\,\hat{\mathbf{z}} \Rightarrow \tag{75}$$

$$\frac{\mathrm{d}B}{\mathrm{d}z} = -\frac{2\lambda B_0 R^{2\lambda} z}{(R^2+z^2)^{\lambda+1}}. \tag{76}$$

Defining a constant $\beta = \mp\dfrac{2\lambda\mu B_0 R^{2\lambda}}{m}$, the equation of motion then becomes

$$\ddot{z} = \gamma + \frac{\beta z}{(R^2+z^2)^{\lambda+1}}. \tag{77}$$

In order to progress the problem, note that

$$g = \dot{z} \Rightarrow \ddot{z} = g\frac{\mathrm{d}g}{\mathrm{d}z}. \tag{78}$$

This then leads to

$$g\frac{\mathrm{d}g}{\mathrm{d}z} = \gamma + \frac{\beta z}{(R^2+z^2)^{\lambda+1}} \Rightarrow \tag{79}$$

$$\frac{g^2}{2} + J_1 = \int\left(\gamma + \frac{\beta z}{(R^2+z^2)^{\lambda+1}}\right)\mathrm{d}z = \gamma z - \frac{\beta}{2\lambda(R^2+z^2)^{\lambda}} + J_2 \Rightarrow \tag{80}$$

$$\dot{z} = g = \sqrt{2\gamma z - \frac{\beta}{\lambda(R^2+z^2)^{\lambda}} + J_3} \Leftrightarrow \mathrm{d}t = \frac{\mathrm{d}z}{\sqrt{2\gamma z - \dfrac{\beta}{\lambda(R^2+z^2)^{\lambda}} + J_3}} \Rightarrow$$

$$t = \int \frac{\mathrm{d}z}{\sqrt{2\gamma z - \dfrac{\beta}{\lambda(R^2+z^2)^{\lambda}} + J_3}}. \tag{81}$$

Here J_n denotes integration constants. It is straightforward to find J_3 from boundary conditions, however, evaluating the integral is proving difficult.

A.2.2   The transverse equations

Letting the magnetic field now be a function of time means that α is also a function of time. As in the previous section, start out by deriving equation (50), rearranging and equating to (51):

$$v_y = \frac{\dot{v}_x}{\alpha} \Rightarrow \dot{v}_y = \frac{\ddot{v}_x}{\alpha} - \frac{\dot{v}_x}{\alpha^2}\dot{\alpha} \Rightarrow \dot{v}_y + \alpha v_x = \frac{\ddot{v}_x}{\alpha} - \frac{\dot{v}_x}{\alpha^2}\dot{\alpha} + \alpha v_x = 0 \Leftrightarrow \ddot{v}_x - \frac{\dot{\alpha}}{\alpha}\dot{v}_x + \alpha^2 v_x = 0. \tag{82}$$

This is a second order, linear, ordinary differential equation with variable coefficients, arranged in a canonical form. Let $v_x(t) = u(t)p(t)$, then (82) can be written as

$$\ddot{p} + \left(\frac{2\dot{u}}{u} - \frac{\dot{\alpha}}{\alpha}\right)\dot{p} + \left(\frac{\ddot{u}}{u} - \frac{\dot{\alpha}}{\alpha}\frac{\dot{u}}{u} + \alpha^2\right)p = 0. \tag{83}$$

Now choose u such that

$$\frac{2\dot{u}}{u} - \frac{\dot{\alpha}}{\alpha} = 0 \Rightarrow \frac{\mathrm{d}}{\mathrm{d}t}\ln\left(u^2\right) = \frac{\mathrm{d}}{\mathrm{d}t}\ln\left(\alpha\right) \Rightarrow u = \sqrt{\alpha}. \tag{84}$$

With this choice of u, equation (83) takes the following form:

$$\ddot{p} + \left(\alpha^2 - \left(\frac{\dot{\alpha}}{2\alpha}\right)^2 + \frac{1}{2}\frac{\mathrm{d}}{\mathrm{d}t}\left(\frac{\dot{\alpha}}{\alpha}\right)\right)p = 0, \qquad \frac{\mathrm{d}}{\mathrm{d}t}\left(\frac{\dot{\alpha}}{\alpha}\right) = \frac{\ddot{\alpha}}{\alpha} - \left(\frac{\dot{\alpha}}{\alpha}\right)^2 \Rightarrow \tag{85}$$

$$\ddot{p} + \left(\alpha^2 - \left(\frac{\dot{\alpha}}{2\alpha}\right)^2 + \frac{\ddot{\alpha}}{2\alpha} - \frac{1}{2}\left(\frac{\dot{\alpha}}{\alpha}\right)^2\right)p = 0 \Leftrightarrow \ddot{p} + \left(\alpha^2 - \frac{3}{4}\left(\frac{\dot{\alpha}}{\alpha}\right)^2 + \frac{\ddot{\alpha}}{2\alpha}\right)p = 0. \tag{86}$$

Separating p and α, this becomes

$$\frac{\ddot{p}}{p} = -\left(\alpha^2 - \frac{3}{4}\left(\frac{\dot{\alpha}}{\alpha}\right)^2 + \frac{\ddot{\alpha}}{2\alpha}\right). \tag{87}$$

Neglecting the deviation from the z-axis once more and defining a constant κ such that

$$\alpha = \frac{qB}{m} = \frac{qB_0}{m}\frac{R^{2\lambda}}{(R^2 + z^2)^\lambda} = \frac{\kappa}{(R^2 + z^2)^\lambda}. \tag{88}$$

The time derivatives can then be written as

$$\dot{\alpha} = -\frac{2\lambda\kappa\dot{z}z}{(R^2 + z^2)^{\lambda+1}}, \qquad \ddot{\alpha} = \frac{2\lambda\kappa}{(R^2 + z^2)^{\lambda+2}}\left((1 + 2\lambda)\dot{z}^2z^2 - \ddot{z}z^3 - R^2\ddot{z}z - R^2\dot{z}^2\right). \tag{89}$$

This means that

$$\frac{\dot{\alpha}}{\alpha} = -\frac{2\lambda\dot{z}z}{R^2 + z^2}, \qquad \frac{\ddot{\alpha}}{2\alpha} = \frac{\lambda}{(R^2 + z^2)^2}\left((1 + 2\lambda)\dot{z}^2z^2 - \ddot{z}z^3 - R^2\ddot{z}z - R^2\dot{z}^2\right). \tag{90}$$

With this in mind, euqation (87) takes the following form:

$$\frac{\ddot{p}}{p} = -\left(\frac{\kappa^2}{(R^2 + z^2)^{2\lambda}} - \frac{3}{4}\left(-\frac{2\lambda\dot{z}z}{R^2 + z^2}\right)^2 + \frac{\lambda}{(R^2 + z^2)^2}\left((1 + 2\lambda)\dot{z}^2z^2 - \ddot{z}z^3 - R^2\ddot{z}z - R^2\dot{z}^2\right)\right). \tag{91}$$

It is possible to proceed from here by substituting in the expressions for $\ddot{z}$ and $\dot{z}$ according to equations (77) and (80). Before doing so, however, drop the subscript from the integration constant and rewrite β in terms of κ, such that

$$J_3 \to J, \qquad \beta = \mp 2\lambda\mu\frac{B_0R^{2\lambda}}{m} = \frac{\mp 2\lambda\mu}{q}\kappa \Rightarrow$$

$$\dot{z}^2 = 2\gamma z \pm \frac{2\mu\kappa}{q(R^2 + z^2)^\lambda} + J, \qquad \ddot{z} = \gamma \mp \frac{2\lambda\mu\kappa z}{q(R^2 + z^2)^{\lambda+1}}. \tag{92}$$

Thus the final expression turns out to be

$$\frac{\ddot{p}}{p} = \tag{93}$$

$$\mp\frac{2\lambda^2\mu\kappa}{q}\frac{z^4 + R^2z}{(R^2 + z^2)^{\lambda+5}} \pm \frac{2\lambda\mu\kappa}{q}\frac{R^2}{(R^2 + z^2)^{\lambda+4}} + \frac{\lambda\left(\gamma z^3 + 2\gamma R^2z + \gamma R^2 + JR^2\right)}{(R^2 + z^2)^4} + \frac{\lambda(\lambda - 1)\left(2\gamma z^3 + Jz^2\right)}{(R^2 + z^2)^2}.$$

It is unclear how to move forward from here, though if the integral in (81) can be evaluated, a solution may follow.

A.3 Falloff exponent and optimal starting position

Looking at the expression for the Stern-Gerlach force, it seems like it is possible to increase the force by simply increasing the falloff rate by, in turn, increasing the exponent λ. Consider the force,

$$F_{SG} = \frac{m\beta z}{\left(R^2 + z^2\right)^{\lambda+1}}. \tag{94}$$

Now let $m\beta z = K\lambda$, $A = R^2 + z^2$ and $R = 1$, then

$$\frac{\mathrm{d}}{\mathrm{d}\lambda} F_{SG} = \frac{\mathrm{d}}{\mathrm{d}\lambda} \frac{K\lambda}{A^{\lambda+1}} = \frac{K}{A^{\lambda+1}} \left(1 - \lambda \ln A\right). \tag{95}$$

Thus, for a given z the greatest force is achieved when $\lambda = \ln^{-1}\left(1 + z^2\right)$. As an example, when the electric field is off and the particle spends the entire flight time around $z = 0.5$, an optimal exponent would be $\lambda = \ln^{-1}(1.25) \approx 4.48$. The force is, in this case, around one and a half times greater than the simple loop current. Hence, it seems that optimizing the exponent will not increase the spin separation even one order of magnitude, though this example alone is not entirely exhaustive.

The height where the force is strongest can be calculated from

$$\frac{\mathrm{d}}{\mathrm{d}z} F_{SG} = \frac{m\beta}{\left(R^2 + z^2\right)^{\lambda+1}} - \frac{2m\beta(\lambda+1)z^2}{\left(R^2 + z^2\right)^{\lambda+2}} = \tag{96}$$

$$\frac{m\beta + m\beta z^2 - 2m\beta\lambda z^2 - 2m\beta z^2}{\left(R^2 + z^2\right)^{\lambda+2}} = \frac{m\beta\left(1 - 2\lambda z^2 - z^2\right)}{\left(R^2 + z^2\right)^{\lambda+2}}.$$

This is zero when

$$(1 + 2\lambda)z^2 - 1 = 0 \Rightarrow z = \frac{1}{\sqrt{1 + 2\lambda}} \ \forall\, z > 0. \tag{97}$$

As such, when the electric field is off and the longitudinal movement of the particle is small, the optimal starting position is $z_0 = 0.5\,\mathrm{m}$ in the case of $\lambda = 3/2$ (a loop current field).

B   Appendix - Code

Presented below is the code used to generate the results. There are some blocks that have been commented out; the program has several features used to troubleshoot, to sanity check the output and to investigate different aspects of the simulation, though they are not needed when gathering the final data. If this program is run on a device with the Python package Numba installed, it is possible to comment in the Numba command above most functions in order to make them run faster.

```python
import numpy as np
import math as math
import matplotlib.pyplot as plt
# from scipy.optimize import curve_fit
# import numba as nb
import time
# from mpl_toolkits.mplot3d.art3d import Poly3DCollection

#Timer to measure runtime.
start_time=time.time()

#Natural constants in SI
muB=9.274*pow(10, -24)
qe=1.602*pow(10, -19)
me=9.109*pow(10, -31)
mp=1.672*pow(10, -27)

#Detector properties
falloff=3/2
E0=0
B0=1
Lfield=1
Ldrift=0
R=1

z_start=0.48
Ltot=Lfield+Ldrift
B_up=np.array([0,0,B0/(z_start**2+R**2)**(3/2)])
B_down=np.array([0,0,B0/(z_start**2+R**2)**(3/2)])

Bgrad_up=-3*z_start*B0*R**2/pow((R**2+z_start**2),5/2)
Bgrad_down=Bgrad_up

E=np.array([0,0,E0])

B_start=B_up[2]
#Detector plate geometry. Here three corners are defined which will be used to
↪   generate the plane.
# p0=np.array([0.05, 0, 0.45])
# p1=np.array([0.05, 0, 0.55])
# p2=np.array([0.15, 0, 0.55])

#Particle properties
m=4*mp
q=qe

# L=0
# S=1/2
```

```python
48    # J=1/2
49    # MJ=1/2
50
51    # landeG=1+(J*(J+1)+S*(S+1)-L*(L+1))/(2*J*(J+1))
52
53    # mu=-landeG*muB*MJ
54
55    mu=-muB
56
57    pos_up=np.array([0,0,0])
58    pos_down=np.array([0,0,0])
59
60    Energy_EV=3000
61    Energy_J=Energy_EV*pow(10,-19)
62    v_start=math.sqrt(2*Energy_J/m)
63
64    vx=v_start
65    vy=0
66    vz=0
67
68    v_up=np.array([vx,vy,vz])
69    v_down=v_up
70
71    #Calculating the electric force outside the loop for efficiency since it is
      ↪   constant.
72    Fe=q*E
73
74    #Step size
75    dt=pow(10, -10)
76
77    #Position, angle and time recorders
78    Prec_up=np.zeros(shape=(1, 3))
79    Thetarec_up=np.array([])
80    Trec_up=np.array([])
81    Radrec_up=np.array([])
82
83    Prec_down=np.zeros(shape=(1, 3))
84    Thetarec_down=np.array([])
85    Trec_down=np.array([])
86    Radrec_down=np.array([])
87
88    #Time of flight
89    T=0
90
91    #Trajectory length
92    S=0
93
94    #Lap separation
95    LapSeps=np.array([])
96    switch=0
97    theta_tol=0.1
98    lap_indeces=np.array([])
99    lap_times=np.array([])
100
101   #Recording parameter
102   N=1
```

```
103
104    #Derivative function used in the Runge-Kutta function
105    # @nb.jit(nopython=True)
106    def derivative(x_speed,y_speed,charge,mass,Efield,Bfield,Bgrad,mag_moment):
107
108        acc_x=charge*y_speed*Bfield[2]/mass
109
110        acc_y=-charge*x_speed*Bfield[2]/mass
111
112        acc_z=charge*Efield/mass+mag_moment*Bgrad/mass
113
114        deriv=np.array([acc_x,acc_y,acc_z])
115        return deriv
116
117    #4th order Runge-Kutta step function which is used to progress the simulation
118    # @nb.jit(nopython=True)
119    def RKstep_v(velocity,charge,mass,Efield,Bfield,Bgrad,mag_moment,timestep):
120
121        slope1=derivative(
122            velocity[0], velocity[1], charge, mass, Efield, Bfield, Bgrad, mag_moment
123        )
124
125        k1x=timestep*slope1[0]
126        k1y=timestep*slope1[1]
127        kz=timestep*slope1[2]
128
129        slope2=derivative(
130            velocity[0]+0.5*k1x, velocity[1]+0.5*k1y, charge, mass, Efield, Bfield,
             ↪ Bgrad, mag_moment
131        )
132
133        k2x=timestep*slope2[0]
134        k2y=timestep*slope2[1]
135
136        slope3=derivative(
137            velocity[0]+0.5*k2x, velocity[1]+0.5*k2y, charge, mass, Efield, Bfield,
             ↪ Bgrad, mag_moment
138        )
139
140        k3x=timestep*slope3[0]
141        k3y=timestep*slope3[1]
142
143        slope4=derivative(
144            velocity[0]+k3x,velocity[1]+k3y, charge, mass, Efield, Bfield, Bgrad,
             ↪ mag_moment
145        )
146
147        k4x=timestep*slope4[0]
148        k4y=timestep*slope4[1]
149
150        vx_new=0
151        vx_new=velocity[0]+(k1x+2*k2x+2*k3x+k4x)/6
152        vy_new=velocity[1]+(k1y+2*k2y+2*k3y+k4y)/6
153        vz_new=velocity[2]+kz
154
155        velocity_new=np.array([vx_new,vy_new,vz_new])
```

```python
156         return velocity_new
157
158    #Fast cross product
159    # @nb.jit(nopython=True)
160    def crossprod(a,b):
161        cross=np.cross(a,b)
162        return cross
163
164    #Fast division
165    # @nb.jit(nopython=True)
166    def division(c,d):
167        quotient=c/d
168        return quotient
169
170    #Fast tangent
171    # @nb.jit(nopython=True)
172    def atan(e,f):
173        tanangle=math.atan2(e,f)
174        return tanangle
175
176    #Fast norm
177    # @nb.jit(nopython=True)
178    def norm(g,h):
179        norm=math.sqrt(g**2+h**2)
180        return norm
181
182    #Fast norm 3D
183    # @nb.jit(nopython=True)
184    def norm3D(i,j,k):
185        norm3D=math.sqrt(i**2+j**2+k**2)
186        return norm3D
187
188    #This function appends a 3D vector to an array. It is used to store all
189    #3D positions for the graph. For some reason it doesn't work with Numba.
190    # @nb.jit(nopython=True)
191    def VectorAppend(SomeArray, AppendixVector):
192        AppendedArray=np.append(SomeArray,AppendixVector,axis=0)
193        return AppendedArray
194
195    #This function appends a scalar to the end of an array.
196    # @nb.jit(nopython=True)
197    def ScalarAppend(SomeArray, AppendixScalar):
198        AppendedArray=np.append(SomeArray,AppendixScalar)
199        return AppendedArray
200
201    #Finding the guiding center outside the loop since it only needs to be calculated
        twice.
202    vtrans=abs(vx)
203    r=m*vtrans/(abs(q)*B_up[2])
204
205    angle_v=math.atan2(vy,vx)
206    if angle_v<0:
207        angle_v=angle_v+2*math.pi
208
209    theta_start=angle_v+3*math.pi/2
210    if theta_start>2*math.pi:
```

```
211         theta_start=theta_start-2*math.pi

212

213    x_center=r*math.cos(theta_start)
214    y_center=r*math.sin(theta_start)

215

216    #Setting the guiding center to the origin. Manually inputting a slight deviation
       ↪  from z=0 in order to not get a zero force.
217    pos_up=np.array([0,np.sign(q)*r,z_start])
218    pos_down=np.array([0,np.sign(q)*r,z_start])

219

220    Prec_up[0]=pos_up
221    Prec_down[0]=pos_down

222

223    #Setting the first index to zero since this is where the first lap starts.
224    lap_indeces=ScalarAppend(lap_indeces,int(0))

225

226    #Generating the plane. Beginning with the basis vectors.
227    # u1=p1-p0
228    # u2=p2-p0
229    # DetectorNormal=crossprod(u1, u2)
230    # DetectorNormal=DetectorNormal/norm3D(DetectorNormal[0], DetectorNormal[1],
       ↪  DetectorNormal[2])
231    # impact=False

232

233    while T<10*pow(10,-6):

234

235        #Position update
236        v_up=RKstep_v(v_up,q,m,E0,B_up,Bgrad_up,mu,dt)
237        dr_up=v_up*dt
238        pos_up=pos_up+dr_up

239

240        v_down=RKstep_v(v_down,q,m,E0,B_down,Bgrad_down,-mu,dt)
241        dr_down=v_down*dt
242        pos_down=pos_down+dr_down

243

244        #Checking if the detector is less that one position step away.
245        # DetectorDistance=abs(np.dot(pos_up-p0,DetectorNormal))
246        # if DetectorDistance<norm3D(dr_up[0],dr_up[1],dr_up[2]) and
       ↪  norm((pos_up[1]-y_center),(pos_up[0]-x_center))>0.045:
247        #     impact=True
248        #     print(DetectorDistance)

249

250        #Updating trajectory length
251        # S=S+norm3D(dr_up[0],dr_up[1],dr_up[2])

252

253        #Updating TOF
254        T=T+dt
255        print(T)
256        print()

257

258        #Recording new position, angle, lap separation and time for plot. Not all
           ↪  positions are recorded for the graph.
259        #This is in order to limit the runtime and to make the plot easier to view.
260        if N%10==0:
261            #Recording position
262            Prec_up=VectorAppend(Prec_up,[pos_up])
```

```
263              Prec_down=VectorAppend(Prec_down,[pos_down])
264
265              #Recording angle
266              theta=atan(pos_up[1],pos_up[0])
267              if theta<0:
268                  theta=theta+2*math.pi
269
270              Thetarec_up=ScalarAppend(Thetarec_up,theta)
271
272              #Recording time
273              Trec_up=ScalarAppend(Trec_up,T)
274
275              #Recording current cyclotron radius
276              radius=norm(pos_up[1],pos_up[0])
277              Radrec_up=ScalarAppend(Radrec_up,radius)
278
279              #As soon as the angle moves outside the tolerance the switch is turned on
     ↪    such that now it is ready to record
280              #when it is within the tolerance again.
281              if switch==0 and abs(Thetarec_up[-1]-theta_start)>theta_tol:
282                  switch=1
283
284              # #When the switch is on and the angle moves within the tolerance, a lap is
     ↪    recorded.
285              if switch==1 and abs(Thetarec_up[-1]-theta_start)<theta_tol:
286                  lap_indeces=ScalarAppend(lap_indeces, len(Trec_up)-1)
287                  last_lap_index=int(lap_indeces[-2])
288                  lap_sep=Prec_up[-1,2]-Prec_up[last_lap_index,2]
289                  LapSeps=ScalarAppend(LapSeps,lap_sep)
290                  lap_times=ScalarAppend(lap_times,T)
291                  switch=0
292
293          #Field update
294          Bnew_up=B0*R**2/((pos_up[2]**2+R**2)**falloff)
295          B_up=np.array([0,0,Bnew_up])
296
297          Bgrad_up=-2*falloff*pos_up[2]*B0*R**2/pow((R**2+pos_up[2]**2),(falloff+1))
298
299          Bnew_down=B0*R**2/((pos_down[2]**2+R**2)**falloff)
300          B_down=np.array([0,0,Bnew_down])
301
302          Bgrad_down=-2*falloff*pos_down[2]*B0*R**2/pow((R**2+pos_down[2]**2),(falloff+1))
303
304          N=N+1
305
306  #Calculating the initial velocities using the formulas derived by Yu-Chen Cheng for
     ↪    comparison.
307  # omega=(q*B0)/m
308  # vx_calc=omega/2*(pos[0]/math.tan((omega*(T-dt))/2)-pos[1])
309  # vy_calc=omega/2*(pos[1]/math.tan((omega*(T-dt))/2)+pos[0])
310  # vz_calc=pos[2]/T-q*E0*T/(2*m)
311
312  # print("Calculated initial velocity according to Yu-Chen Cheng (x,y,z):")
313  # print(vx_calc)
314  # print(vy_calc)
315  # print(vz_calc)
```

```
316    # print()
317    # print("Number of data points:")
318    # print(len(Prec_up[:,1]))
319    # print()
320    print("Runtime (seconds):")
321    runtime=time.time()-start_time
322    print(str(math.floor(runtime/60))+' minute(s) and '+str(runtime%60)+' seconds')
323    print()
324    # print("Guiding center (x,y):")
325    # print(x_center)
326    # print(y_center)
327    # print()
328    print("Initial and final B-field strength:")
329    print(B_start)
330    print(B_up[2])
331    print()
332    print("Final spin separation:")
333    print(pos_up[2]-pos_down[2])
334    print()
335    print("Position of spin up (x,y,z):")
336    print(pos_up[0])
337    print()
338    print(pos_up[1])
339    print()
340    print(pos_up[2])
341    print()
342    print("Position of spin down (x,y,z):")
343    print(pos_down)
344    print()
345    print("TOF:")
346    print(T)
347    print()
348    print("Initial and final radius:")
349    print(norm(Prec_up[0,0],Prec_down[0,1]))
350    print(norm(pos_up[0],pos_up[1]))
351    print()
352    # print("Final lap separation:")
353    # print(LapSeps[-1])
354    # print()
355    # print("Number of completed laps:")
356    # print(len(LapSeps)-1)
357    # print()
358
359    #Plotting the path of the particle. Display in a separate window in order to
360    #interract with the graph.
361    plt.figure(1)
362    ax=plt.axes(projection='3d')
363    ax.set_xlabel('x (cm)')
364    ax.set_ylabel('y (cm)')
365    ax.set_zlabel('z (cm)-0.5 m')
366    # ax.set_xlim3d(-0.25, 0.25)
367    # ax.set_ylim3d(-0.25, 0.25)
368    # ax.set_zlim3d(0, 0.5)
369    ax.plot3D(Prec_up[:, 0]*100, Prec_up[:, 1]*100,(Prec_up[:, 2]-0.5)*100,
       ↪  color='blue')
```

```python
370  ax.plot3D(Prec_down[:, 0]*100, Prec_down[:, 1]*100,(Prec_down[:, 2]-0.5)*100,
     ↪  color='red')
371  #Plotting the detector plate
372  # d_x = [-0.04,-0.04,-0.14,-0.14]
373  # d_y = [0,0,0,0]
374  # d_z = [0.35,0.45,0.45,0.35]
375  # verts = [list(zip(d_x,d_y,d_z))]
376  # ax.add_collection3d(Poly3DCollection(verts,facecolors='black',alpha=0.5))
377
378  # plt.figure(2)
379  # plt.ylabel('Radius')
380  # plt.xlabel('Time')
381  # plt.plot(Trec_up,Radrec_up,'-', markersize=0.6)
382  # plt.legend()
383
384  # plt.figure(3)
385  # plt.ylabel('Lap separation')
386  # plt.xlabel('Time')
387  # plt.plot(lap_times, LapSeps,'-')
388  # plt.legend()
```